

Fine-grained dual-phase high-entropy ceramics derived from boro/carbothermal reduction

Si-Chun Luo

Guangdong University of Technology

Wei-Ming Guo (✉ guo1237@126.com)

Guangdong University of Technology

Kevin Plucknett

Dalhousie University

Hua-Tay Lin

Guangdong University of Technology

Research Article

Keywords: Dual-phase high-entropy ceramics; Boro/carbothermal reduction; Densification; Microstructure; Mechanical properties

Posted Date: August 17th, 2020

DOI: <https://doi.org/10.21203/rs.3.rs-58173/v1>

License: © ⓘ This work is licensed under a Creative Commons Attribution 4.0 International License.

[Read Full License](#)

Version of Record: A version of this preprint was published at Journal of the European Ceramic Society on June 1st, 2021. See the published version at <https://doi.org/10.1016/j.jeurceramsoc.2020.12.044>.

Abstract

In the current work fine-grained dual-phase, high-entropy ceramics $(\text{Ti}_{0.2}\text{Zr}_{0.2}\text{Hf}_{0.2}\text{Nb}_{0.2}\text{Ta}_{0.2})\text{B}_2$ - $(\text{Ti}_{0.2}\text{Zr}_{0.2}\text{Hf}_{0.2}\text{Nb}_{0.2}\text{Ta}_{0.2})\text{C}$ with different phase ratios are prepared from powders synthesized via a boro/carbothermal reduction approach, by adjusting the content of B_4C and C in the precursor powders. Phase compositions, densification, microstructure, and mechanical properties have been investigated. Due to the combination of pinning effect and the boro/carbothermal reduction approach, the average grain sizes (0.5–1.5 μm) of the dual-phase high-entropy ceramics, were much smaller as compared with previously reported values. The dual-phase high-entropy ceramics with 15 mol% boride phase exhibit the highest Vickers hardness (24.21 GPa) and fracture toughness (3.2 $\text{MPa}\cdot\text{m}^{1/2}$).

1. Introduction

In 2015, an entropy stabilized oxide ceramic was reported for the first time, which exhibited a single-phase rock salt structure [1]. Since then, the concept of high-entropy materials has applied to the field of ceramics more widely. In the last two to three years, high-entropy ceramics have become a major global research emphasis. Different series of high-entropy ceramics, such as silicides [2, 3], oxides [1, 4], nitrides [5], carbides [6–9], and borides [10–13] have been widely studied. The subject of high-entropy boride (HEB) and high-entropy carbide (HEC) ceramics are, so far, the most intensively researched.

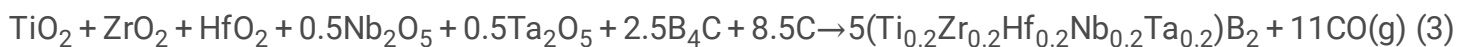
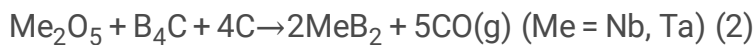
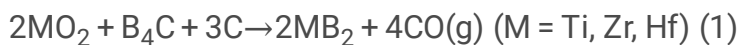
Equiatomic five (or four)-metal HEB and HEC ceramics of transition metal (group IVB, VB, and VB) have the AlB_2 structure (space group $\text{P6}/\text{mmm}$ #191) and rock salt structure (space group Fm-3m #225), respectively. HEB ceramics are known to be difficult to achieve full density, due to the strong, primarily covalent chemical bonds that lead to slow diffusion rates [10]. Six different high-entropy borides were fabricated via high-energy ball milling and spark plasma sintering, whereas the relative density reported was only about 92% [11]. Many researchers have shown that HEC ceramics have lower thermal conductivity, and higher elastic modulus and hardness values as compared to monocarbides. Yan et al. [6] have synthesized $(\text{Hf}_{0.2}\text{Zr}_{0.2}\text{Ta}_{0.2}\text{Nb}_{0.2}\text{Ti}_{0.2})\text{C}$ by spark plasma sintering (SPS), which showed much lower thermal diffusivity and conductivity than the binary carbides like HfC , ZrC , TaC , and TiC . In prior work, most of the HEC and HEB ceramics were fabricated through the use of blends of commercially available single boride or carbide powders, and subsequent *in-situ* HEB or HEC formation during densification [6, 8–9]. As an alternative, high-entropy ceramics can be prepared and sintered using high-entropy powders derived by the boro/carbothermal reduction approach, using metal oxides as powder precursors. For example, a single-phase rock salt structure $(\text{Hf,Zr,Ti,Ta,Nb})\text{C}$ powder was prepared by carbothermal reduction with an average particle size of about 550 nm and an associated oxygen content of 0.2 wt% [14]. Wei et al. [15] prepared $(\text{Ti}_{0.2}\text{Zr}_{0.2}\text{Nb}_{0.2}\text{Ta}_{0.2}\text{W}_{0.2})\text{C}$ ceramic with a relative density up to 99.9%, using metal oxides as powder precursors. Similarly, $(\text{Ti}_{0.2}\text{Hf}_{0.2}\text{Zr}_{0.2}\text{Nb}_{0.2}\text{Ta}_{0.2})\text{B}_2$ ceramics with a relative density of 97.9% were obtained after spark plasma sintering of boro/carbothermal-derived HEB powders at 2050 °C under 50 MPa applied pressure [16]. A series of studies have demonstrated that high-entropy ceramic powders prepared by using the boro/carbothermal reduction approach exhibited better

sintering behavior than the commercial powders [17–19]. Huo et al. showed that a (Ti,Zr)B₂-(Zr,Ti)C composite fabricated by reactive hot pressing can refine the grain size and improve the mechanical properties [20, 21]. Recently, dual-phase high-entropy ultrahigh temperature ceramics (DPHE-UHTCs) have been fabricated starting from a combination of n binary borides and (5-n) binary carbides powders [22]. The relative density of this dual-phase high-entropy ceramic is up to 99%. However, the mean grain sizes of the boride and carbide formed in these dual-phase high-entropy ceramics were larger than 4.2 and 4.9 μm, respectively.

In the present work, (Ti_{0.2}Zr_{0.2}Hf_{0.2}Nb_{0.2}Ta_{0.2})B₂-(Ti_{0.2}Zr_{0.2}Hf_{0.2}Nb_{0.2}Ta_{0.2})C dual-phase high-entropy ceramics were prepared using dual-phase high-entropy powders, which were *in-situ* synthesized by boro/carbothermal reduction approach using oxide precursors. The phase compositions, densification behavior, mechanical properties, and microstructures of the dual-phase high-entropy ceramics were studied. The objective of this study is to provide insight into the feasibility of fabrication of fine-grained dual-phase high-entropy ceramics in order to enhance its mechanical properties based upon applying a low-cost boro/carbothermal reduction approach.

2. Experimental Procedure

Commercially available TiO₂ (~ 21 nm, XuanchengJingrui New Material Co., Ltd.), ZrO₂ (~ 0.6 μm, ChangshaXili Nanometer Lapping Tech. Co., Ltd.), HfO₂ (~ 0.3 μm, BeijingFounde Star Sci. & Tech. Co., Ltd.), Nb₂O₅ (~ 2.0 μm, Beijing Founde Star Sci. & Tech. Co, Ltd.), Ta₂O₅ (~ 1.0 μm, Beijing Founde Star Sci. & Tech. Co., Ltd.), B₄C (~ 1 μm, Mudanjiang Jingangzuan Boron Carbide Co., Ltd.), and graphite (~ 1.5 μm, Shanghai Yifan Graphite Co., Ltd.) powders were used as the initial raw materials in this study. The reactions of using oxides, B₄C and C as precursors to prepare high-entropy borides and carbides powders are as follows:



However, it should be noted that, a large number of researches have shown that when borides are prepared with the stoichiometric amounts of raw powders, according to Reactions (1), (2) and (3), a small amount of residual oxides would invariably remain in the product [10, 16, 18, 23]. This is due to the evaporation of intermediate gas products (i.e., B₂O₃ and boron-rich oxides), resulting in the loss of B from

the initial mixture. In order to obtain two-phase high-entropy ceramics with different high-entropy phase fractions, the amounts of B_4C and C were thus adjusted in the present work. For the current study, samples with nominally 100 mol% HEB, 80 mol% HEB + 20 mol% HEC, 60 mol% HEB + 40 mol% HEC, 40 mol% HEB + 60 mol% HEC, 20 mol% HEB + 80 mol% HEC, 100 mol% HEC sintered samples are referred to as HEB, B8C2, B6C4, B4C6, B2C8, and HEC, respectively.

Table 1
Precursor powder molar ratios.

Label	TiO ₂ (mol)	ZrO ₂ (mol)	HfO ₂ (mol)	Nb ₂ O ₅ (mol)	Ta ₂ O ₅ (mol)	B ₄ C(mol)	C(mol)
HEB	1	1	1	0.5	0.5	3.125	5.95
H8C2	1	1	1	0.5	0.5	2.5	7.96
H6C4	1	1	1	0.5	0.5	1.875	9.97
H4C6	1	1	1	0.5	0.5	1.25	11.98
H2C8	1	1	1	0.5	0.5	0.625	13.99
HEC	1	1	1	0.5	0.5	0	16

For boro/carbothermal synthesis, the ratio details of these mixes of powders are presented in Table 1. The raw materials were mixed in anhydrous ethanol with Si₃N₄ milling media for 24 hours, using a roll jar mill, and then dried within a rotary evaporator. The dried mixtures were subsequently passed through a 100-mesh sieve to remove any large agglomerates. The powder mixture was then compacted into 30 mm diameter and ~ 5 mm thickness monoliths, and loaded in a graphite crucible. The preparation of the *in-situ* synthesized, boro/carbothermal reduction powder is then carried out in a vacuum furnace. The mixtures were heat treated at 1650°C for 1 h under vacuum (≈ 10 Pa), with a heating rate of 10 °C/min, to complete the boro/carbothermal reaction(s) process. The as-prepared high-entropy powders were subsequently ground with an agate mortar and pestle, and then through a 100-mesh sieve. For powder densification, Spark Plasma Sintering (SPS, HPD-10-FL, FCT Systeme GmbH, Germany) consolidation was conducted, using a graphite die with an inner diameter of 30 mm. All samples were sintered at 2000 °C for 10 min, with a heating rate of 100 °C/min, in an Ar atmosphere. A uniaxial pressure of 30 MPa was applied above 1650°C, and then maintained for the remainder of the sintering cycle.

Bulk densities of the sintered compacts were measured using the Archimedes method in distilled water. The Vickers hardness (ISO 14705: 2008, MOD) was measured by the indentation method, with an applied load of 0.2 kg, held for 10 s. The fracture toughness, K_{IC} , was measured by the indentation method with an applied load of 2 kg, held for 10 s [24]. Crystalline phases within the sintered specimens were determined by X-ray diffractometry (XRD; model D8 ADVANCE, Bruker Corp., Germany). The Rietveld refinement approach was used to calculate the lattice parameters and phase fraction of the high-entropy ceramics from the recorded XRD pattern, using the Rietveld refinement EXPGUI software. The microstructures of SPS processed samples were examined using scanning electron microscopy (SEM;

model SU-8220, Hitachi High-Technologies, Japan), which is equipped with an energy dispersive spectroscopy (EDS) Si-drift detector (X-Max^N50, Oxford, UK) for chemical analysis and mapping.

3. Results And Discussion

3.1 Phase compositions and densification

XRD patterns of all of the sintered samples are shown in Fig. 1. Only single phases of either a hexagonal lattice (nominally corresponding to HfB₂) or face-centred cubic lattice (nominally corresponding to HfC) were detected in the SPS densified HEB and HEC ceramics, respectively. In contrast, the B8C2, B6C4, B4C6, and B2C8 high-entropy ceramic composites are composed of a combination of boride and carbide phases as anticipated. No secondary phases were detected in all any of the SPS densified samples. The XRD results show that using a suitable combination metal oxides, B₄C, and graphite as precursors, synthesis of both single-phase and dual-phase high-entropy ceramics is feasible via boro/carbothermal approach. For the dual-phase B8C2 to B2C8 sequence of samples, the changes in XRD peak intensities are consistent with the changes in the boride (or carbide) phase fraction. This indicates that the high-entropy boride (or carbide) phase fraction in these dual-phase high-entropy ceramics can be carefully tailored through adjustment of the content of B₄C and C.

Considering that the actual phase molar fraction in the sintered dual-phase high-entropy ceramics may not be consistent with the nominal molar fraction, it is necessary to calculate the action fractions of the high-entropy boride phase in the dual-phase ceramics utilizing Rietveld XRD refinement. The molar fraction of the (Ti_{0.2}Zr_{0.2}Hf_{0.2}Nb_{0.2}Ta_{0.2})B₂ phase in dual-phase high-entropy ceramic was calculated from the recorded XRD pattern, as shown in Table 2. The nominal molar fractions for the (Ti_{0.2}Zr_{0.2}Hf_{0.2}Nb_{0.2}Ta_{0.2})B₂ phase in compositions B8C2, B6C4, B4C6, and B2C8 are 80 mol%, 60 mol%, 40 mol%, and 20 mol%, respectively. The actual molar fractions within B8C2, B6C4, B4C6, and B2C8 are 90 mol%, 59 mol%, 35 mol%, and 15 mol%, respectively. The reason for this discrepancy is that it is difficult to accurately quantify the evaporation of gas (i.e., B₂O₃ and rich-boron oxides) during the high-entropy powder preparation step, when using boro/carbothermal reduction. Therefore, as a consequence, the targeted molar ratios of raw powders (specifically, the contents of B₄C and C) needs an increased theoretical and experimental verification to obtain accurate final phase fractions in dual-phase high-entropy ceramics.

Table 2
The calculated boride content and densities of sintered samples.

Label	Boride content mol.%	Theoretical density (g/cm ³)	Relative density (%)
HEB	100	8.23	97.8
B8C2	90	8.33	96.8
B6C4	59	8.64	99.7
B4C6	35	8.91	99.1
B2C8	15	9.17	99.4
HEC	0	9.37	98.7

Based on the recorded XRD patterns for the HEB and HEC ceramics, lattice parameters could be determined for the individual phases. The lattice of the HEB phase were refined as: $a = b = 3.1057 \text{ \AA}$, $c = 3.3794 \text{ \AA}$. The theoretical density of HEB is then calculated to be 8.23 g/cm^3 , which is very consistent with published literature results (i.e., 8.24 g/cm^3) [16]. Similarly, the lattice parameters for the HEC phase were refined as: $a = b = c = 4.521 \text{ \AA}$. The theoretical density of HEC is then calculated to be 9.37 g/cm^3 , very consistent with literature data (i.e., 9.39 g/cm^3) [6]. The theoretical density of the dual-phase ceramics can be then calculated according to the rule of mixtures, based on the theoretical densities of the respective HEB and HEC phases. The measured density of all of the SPS processed high-entropy ceramic composite samples is presented in Table 2. The relative densities of HEB, B8C2, B6C4, B4C6, B2C8, and HEC are 97.8%, 96.8%, 99.7%, 99.1%, 99.4%, and 98.7%, respectively. Further analysis of the determined density values would be provided below.

3.2 Microstructure Characterization

SEM images in backscattering mode of the polished surfaces of the SPS densified specimens are shown in Fig. 2. Based on the difference in the mean atomic number, the black and gray contrast phases in the B8C2, B6C4, B4C6, and B2C8 samples (Fig. 2) are $(\text{Ti}_{0.2}\text{Zr}_{0.2}\text{Hf}_{0.2}\text{Nb}_{0.2}\text{Ta}_{0.2})\text{B}_2$ and $(\text{Ti}_{0.2}\text{Zr}_{0.2}\text{Hf}_{0.2}\text{Nb}_{0.2}\text{Ta}_{0.2})\text{C}$, respectively. The associated EDS elemental mapping for Ti, Zr, Hf, Nb, and Ta, in this case for sample B4C6, are presented in Fig. 3. Results show that there is no indication of notable clustering or segregation is visible within the individual element maps of B4C6, suggesting that these metal elements formed a solid solution in each HEB and HEC phase.

Microstructures of the fracture surfaces of the sintered specimens are shown in Fig. 4. Some small pores were observed within the grains and at the grain boundaries for the HEB, B8C2, HEC samples (e.g., Fig. 3a, 3b, 3f, 4a, 4b, and 4f). Conversely, no obvious evidence of pores was found in the B6C4, B4C6, or B2C8 samples. These results are consistent with the relative density values of the sintered specimens (Shown previously in Table 2). Based on SEM images of both the polished and fracture surfaces of the HEB, B8C2, and HEC samples (Figs. 3 and 4), an exaggerated grain growth could be observed relative to the

other samples. This rapid grain growth could lead to the formation of intragranular porosity, which becomes difficult to remove, and then inhibited full densification. However, due to the mutual grain-boundary pinning effect, the dual-phase ceramics with a more even ratio of boride to carbide have finer grain size and significantly less residual porosity. The fracture morphology of the single-phase high-entropy boride (HEB) samples was transgranular in nature (Fig. 4a), indicating a strong interface is formed between the individual high-entropy boride grains. However, in contrast, the fracture morphology of the single-phase high-entropy carbide (HEC) was intergranular in character (Fig. 5f). In further comparison, the dual-phase high-entropy ceramics containing both the high-entropy boride and carbide phases, showed both transgranular and intergranular fracture features (i.e., a mixed fracture model).

The variations in the grain sizes of the carbide and boride phases, as a function of the overall composition in the sintered samples, and hence the respective phase fraction, are presented in Fig. 5. The average grain sizes of the HEB and HEC samples are 2.58 μm and 2.31 μm , respectively. Due to the grain pinning effects, the grain size of the dual-phase high-entropy ceramics showed obvious mutual growth, inhibition, and each phase was smaller than that of the respective single-phase carbide and boride high-entropy ceramics. The grain size decreased with the increase in counterpart phase fraction, similar to results previously reported in the literature [22]. The B8C2 and B2C8 samples have the smallest carbide and boride grain sizes of 0.53 μm and 0.64 μm , respectively. However, Huo et al. [22] used blended mixtures of commercial borides (TiB_2 , ZrB_2 , NbB_2 , HfB_2 , and TaB_2) and carbides (TiC , ZrC , NbC , HfC , and TaC) as raw materials to prepare high-entropy dual-phase ceramics; this work achieved minimum carbide and boride average grain sizes of 4.9 μm (for the equivalent of the 8B2C formulation) and 4.2 μm (for the equivalent of the 2B8C formulation), respectively. In the present work, the grain sizes of the dual-phase were significantly decreased for high-entropy ceramics composites SPS densified using 'pre-alloyed' powders, *in-situ* synthesized using a simple and low-cost boro/carbothermal reduction approach.

3.3 Mechanical properties

The hardness and toughness of dual-phase high-entropy ceramics with different phase fractions are presented in Fig. 6. Compared to the other samples, HEB shows the lowest hardness of 21.27 GPa, similar to Zhang and colleague's reported value (i.e., 21.7 GPa) [18]. With an increase of the carbide phase content in the dual-phase high-entropy ceramics, the hardness increases, and the B2C8 sample reaches a maximum hardness of 24.21 GPa. Due to the larger grain size, the hardness of the HEC samples (23.13 GPa) is slightly lower than that of B2C8.

The change in trend of indentation fracture toughness with carbide content is similar to the hardness. The toughness of HEB, B8C2, B6C4, B4C6, B2C8, and HEC are 2.34 $\text{MPa}\cdot\text{m}^{1/2}$, 2.39 $\text{MPa}\cdot\text{m}^{1/2}$, 2.72 $\text{MPa}\cdot\text{m}^{1/2}$, 2.76 $\text{MPa}\cdot\text{m}^{1/2}$, 3.19 $\text{MPa}\cdot\text{m}^{1/2}$, and 3.04 $\text{MPa}\cdot\text{m}^{1/2}$, respectively. With the increase in the carbide phase content in the present dual-phase high-entropy ceramics, the toughness increases. The fracture toughness is related to the fracture model. As shown previously in Fig. 4, the boride phase showed a transgranular fracture model, whereas the carbide phase exhibited a the predominantly intergranular fracture model. The occurrence of intergranular fracture demonstrates the existence of some operative toughening mechanisms (e.g., crack deflection, residual stress, etc.), resulting in higher

measured toughness values. The toughness value of the HEC sample is slightly smaller than that of B2C8, potentially due to the grain growth in the single-phase HEC, from 1.47 to 2.31 μm .

4. Conclusions

Using a mixture of metal oxides, B_4C and graphite powders as precursors, single-phase high-entropy boride, and carbide ceramic powders, together with dual-phase high-entropy powders, were synthesized via a simple one-step boro/carbothermal reduction approach. A series of high density, dual-phase high-entropy ceramics, with different boride to carbide phase ratios, were then obtained by SPS processing at 2000°C. Compared to previously reported mean grain size values for similar dual-phase high-entropy materials processed from mixtures of single element commercial boride and carbide powders, the averaged grain sizes of high-entropy dual-phase ceramics in the present work are significantly reduced, by roughly one order of magnitude. For the SPS processed samples in the current work, dual-phase high-entropy ceramics with 15 mol% of the boride phase exhibit the highest Vickers hardness (24.21 GPa) and fracture toughness ($3.2 \text{ MPa}\cdot\text{m}^{1/2}$).

Declarations

Acknowledgments

This work was financially supported by National Natural Science Foundation of China (No. 51832002, 51402055, 51602060 and U1401247).

References

1. Rost CM, Sachet E, Borman T, *et al.* Entropy-stabilized oxides. *Nat Commun* 2015, 6: 8485.
2. Gild J, Braun J, Kaufmann K, *et al.* A High-Entropy Silicide: $(\text{Mo}_2\text{Nb}_{0.2}\text{Ta}_{0.2}\text{Ti}_{0.2}\text{W}_{0.2})\text{Si}_2$. *J Materiomics* 2019, 5: 337-343.
3. Qin Y, Liu JX, Li F, *et al.* A high entropy silicide by reactive spark plasma sintering. *J Adv Ceram* 2019, 8:148-152.
4. Dąbrowa J, Stygar M, Mikuła A, *et al.* Manfred Martin. Synthesis and microstructure of the $(\text{Co,Cr,Fe,Mn,Ni})_3\text{O}_4$ high entropy oxide characterized by spinel structure. *Mater Lett* 2018, 216: 32-36.
5. Jin T, Sang XH, Unocic RR, *et al.* Mechanochemical-Assisted Synthesis of High-Entropy Metal Nitride via a Soft Urea Strategy. *Adv Mater* 2018, 30: 1707512.
6. Yan XL, Constantin L, Lu YF, *et al.* $(\text{Hf}_2\text{Zr}_{0.2}\text{Ta}_{0.2}\text{Nb}_{0.2}\text{Ti}_{0.2})\text{C}$ high-entropy ceramics with low thermal conductivity. *J Am Ceram Soc* 2018, 101: 4486-4491.
7. Ye BL, Wen TQ, Chu YH. High-temperature oxidation behavior of $(\text{Hf}_2\text{Zr}_{0.2}\text{Ta}_{0.2}\text{Nb}_{0.2}\text{Ti}_{0.2})\text{C}$ high-entropy ceramics in air. *J Am Ceram Soc* 2020, 103: 500–507.

8. Ye BL, Wen TQ, Liu D, *et al.* Oxidation behavior of $(\text{Hf}_2\text{Zr}_{0.2}\text{Ta}_{0.2}\text{Nb}_{0.2}\text{Ti}_{0.2})\text{C}$ high-entropy ceramics at 1073-1473 K in air. *Corros Sci* 2019, 153: 327-332.
9. Gorban' VF, Andreyev AA, Kartmazov GN, *et al.* Production and mechanical properties of high-entropic carbide based on the TiZrHfVNbTa multicomponent alloy. *J Superhard Mater* 2017, 39: 166-171.
10. Gild J, Wright A, Quiambao-Tomko K, *et al.* Thermal conductivity and hardness of three single-phase high-entropy metal diborides fabricated by borocarbothermal reduction and spark plasma sintering. *Ceram Int* 2020, 46: 6906-6913.
11. Gild J, Zhang YY, Harrington T, *et al.* High-Entropy Metal Diborides: A New Class of High-Entropy Materials and a New Type of Ultrahigh Temperature Ceramics. *Sci Rep* 2016, 6: 37946.
12. Liu D, Liu HH, Ning SS, *et al.* Chrysanthemum-like high-entropy diboride nanoflowers: A new class of high-entropy nanomaterials. *J Adv Ceram* 2020, 9:339-348.
13. Liu JX, Shen XQ, Wu Y, *et al.* Mechanical properties of hot-pressed high-entropy diboride-based ceramics. *J Adv Ceram* 2020, 9: 503-510.
14. Lun F, Fahrenholtz WG., Hilmas GE, *et al.* Synthesis of single-phase high-entropy carbide powders. *Scr Mater* 2019, 162: 90-93.
15. Wei XF., Liu JX., Li F, *et al.* High entropy carbide ceramics from different starting materials. *J Eur Ceram Soc* 2019, 39: 2989-2994.
16. Gu JF, Zou J, Sun SK, *et al.* Dense and pure high-entropy metal diboride ceramics sintered from self-synthesized powders via boro/carbothermal reduction approach. *Sci China Mater* 2019, 62: 1898-1909.
17. Zhang Y, Guo WM, Jiang ZB, *et al.* Dense high-entropy boride ceramics with ultra-high hardness. *Scr Mater* 2019, 164: 135-139.
18. Zhang Y, Jiang ZB, Sun SK, *et al.* Microstructure and mechanical properties of high-entropy borides derived from boro/carbothermal reduction. *J Eur Ceram Soc* 2019, 39: 3920-3924.
19. Zhang Y, Sun SK, Zhang W, *et al.* Improved densification and hardness of high-entropy diboride ceramics from fine powders synthesized via borothermal reduction process. *Ceram Int* 2020, 46: 14299-14303.
20. Huo SJ, Wang YJ, Yao MY, *et al.* Reactive sintering behavior and enhanced densification of $(\text{Ti,Zr})\text{B}_2$ - $(\text{Zr,Ti})\text{C}$ composites. *J Eur Ceram Soc* 2020, 40: 4373-4380.
21. Huo SJ, Wang YJ, Kong QY, *et al.* In situ reaction and solid solution induced hardening in $(\text{Ti,Zr})\text{B}_2$ - $(\text{Zr,Ti})\text{C}$ composites. *J Am Ceram Soc* 2020, <https://doi.org/10.1111/jace.17355>.
22. Qin MD, Gild J, Hu CZ, *et al.* Dual-Phase High-Entropy Ultra-High Temperature Ceramics. *J Eur Ceram Soc* 2020, <https://doi.org/10.1016/j.jeurceramsoc.2020.05.040>.
23. Guo WM, Zhang GJ, Reaction Processes and Characterization of ZrB_2 Powder Prepared by Boro/Carbothermal Reduction of ZrO_2 in Vacuum. *J Am Ceram Soc* 2009, 92: 264-267.
24. Evans AG, Charles EA. Fracture Toughness Determinations by Indentation. *J Am Ceram Soc* 1976, 59: 371-372.

Figures

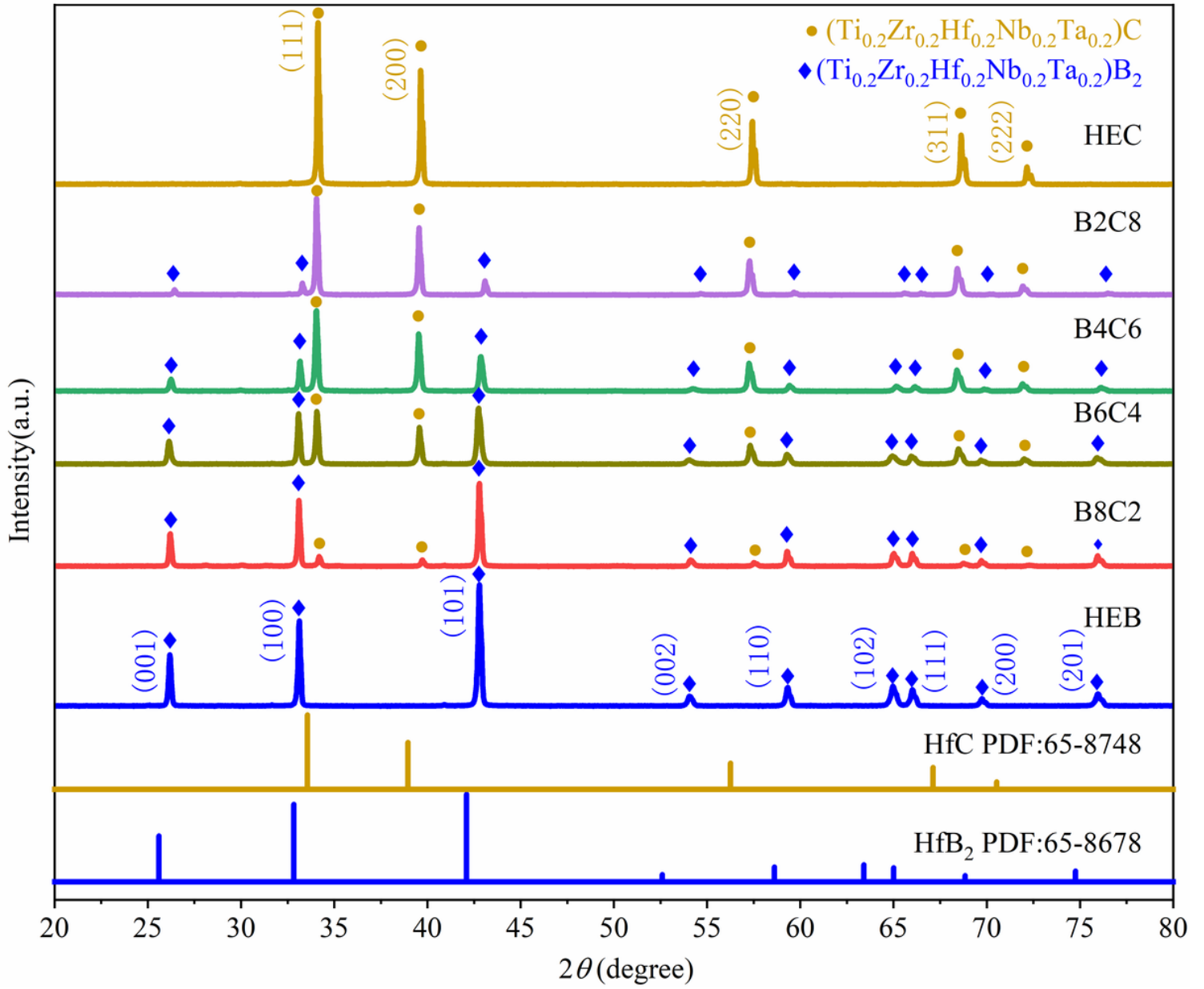


Figure 1

Representative XRD patterns of samples after SPS process.

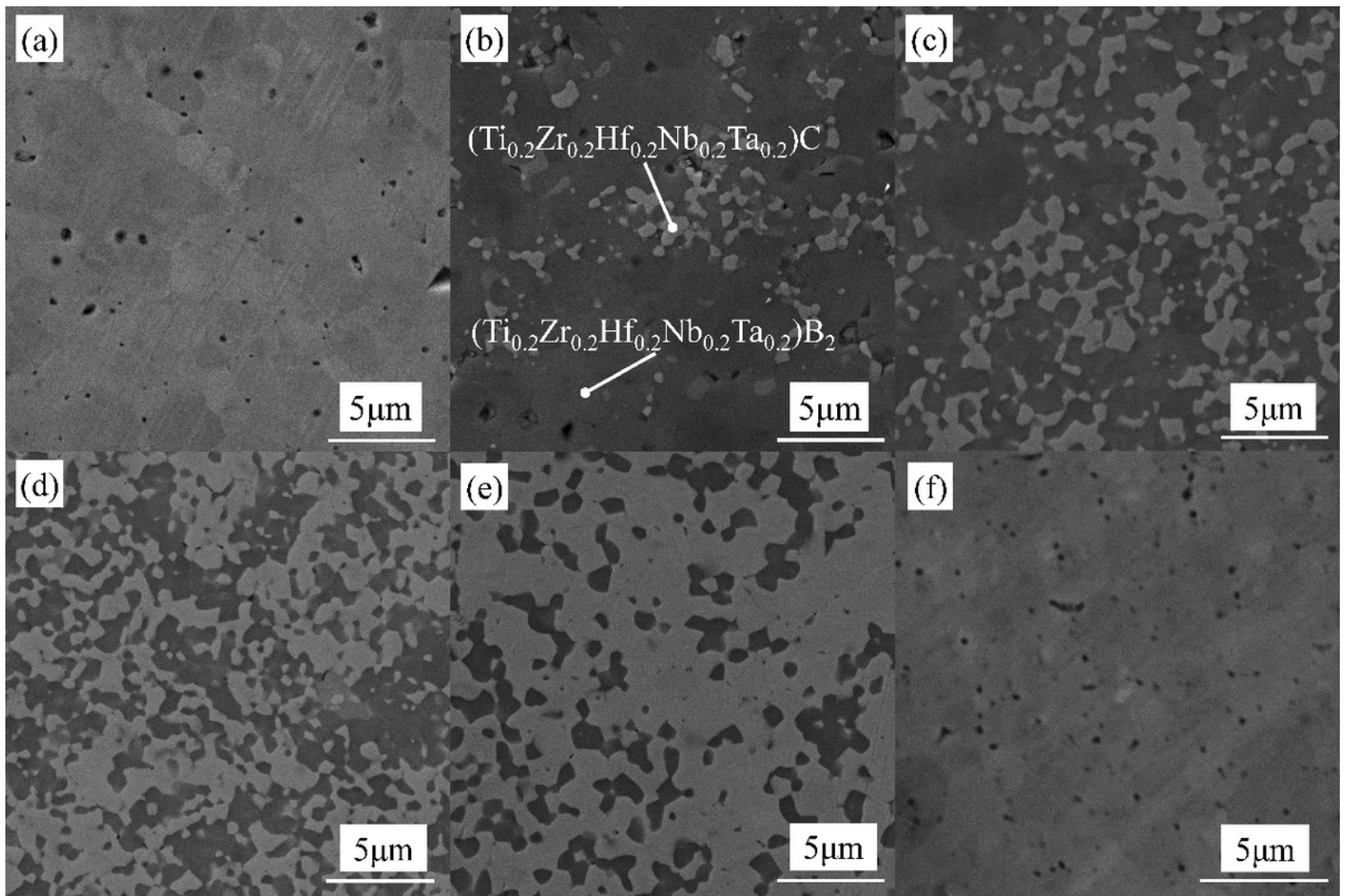


Figure 2

Backscattered electron SEM images of the polished surface of the sintered samples: (a) HEB, (b) B8C2, (c) B6C4, (d) B4C6, (e) B2C8, and (f) HEC.

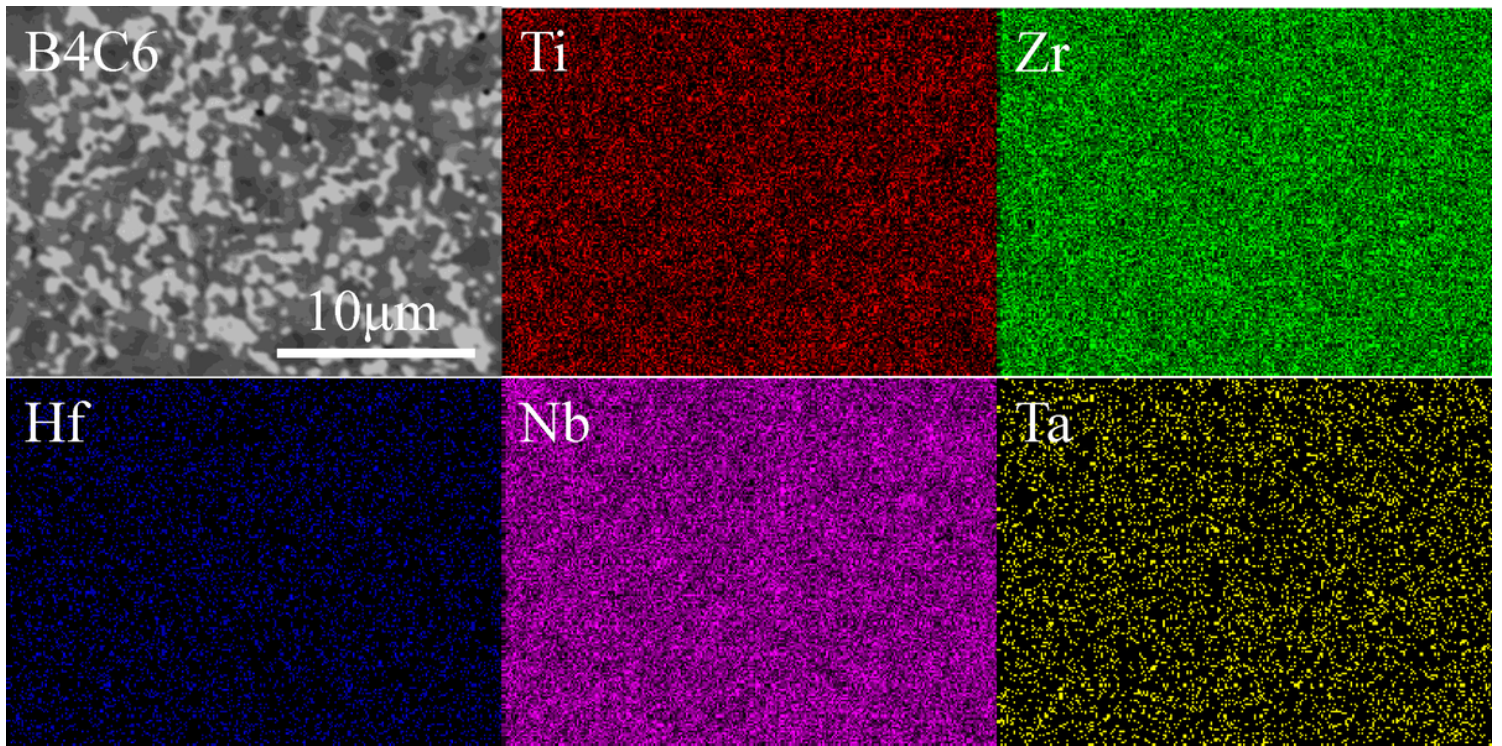


Figure 3

Backscatter electron image and the corresponding EDS elemental mapping for the B4C6 sample.

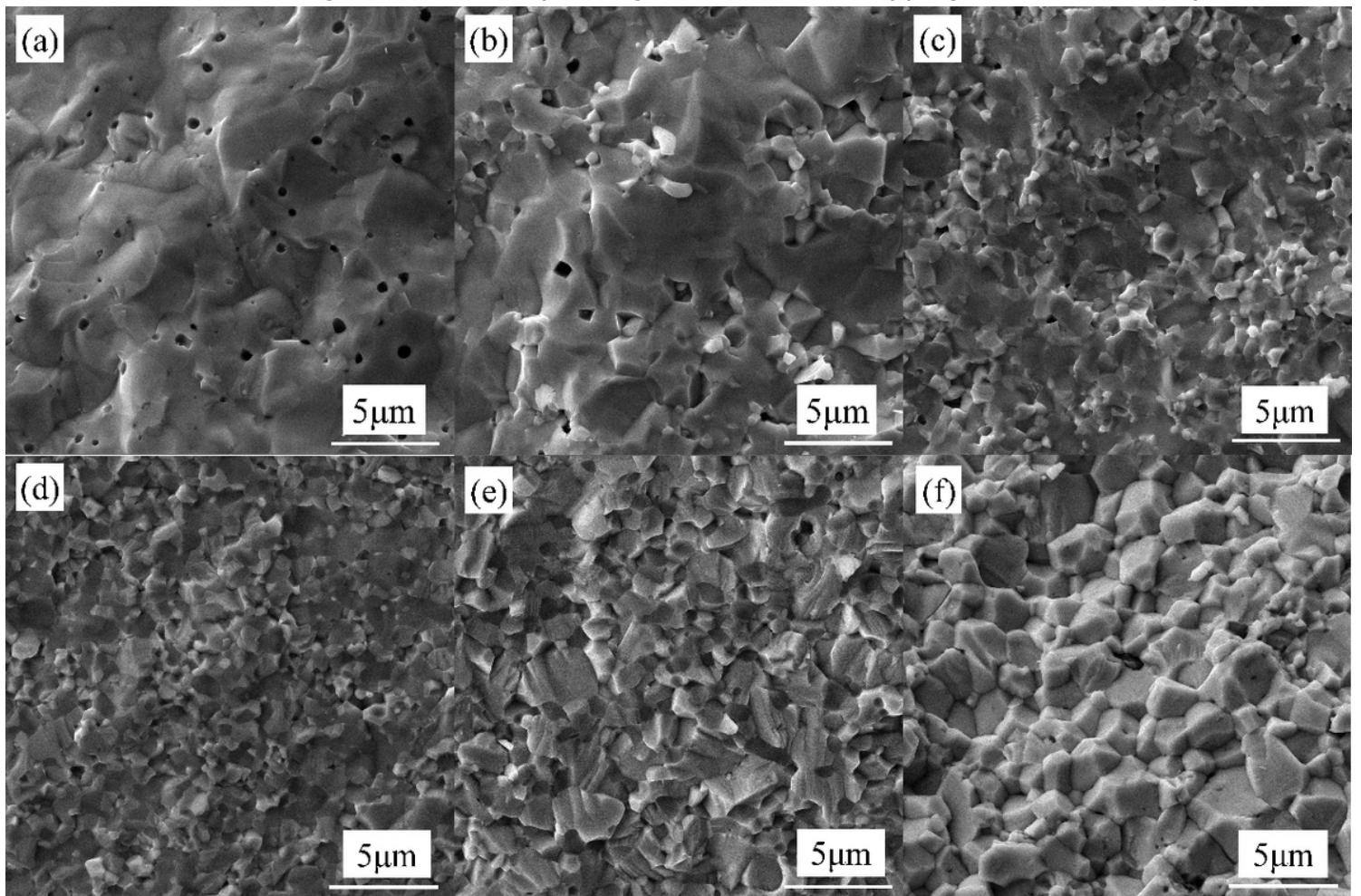


Figure 4

Microstructures of the fracture surfaces of the sintered samples: (a) HEB, (b) B8C2, (c) B6C4, (d) B4C6, (e) B2C8, and (f) HEC.

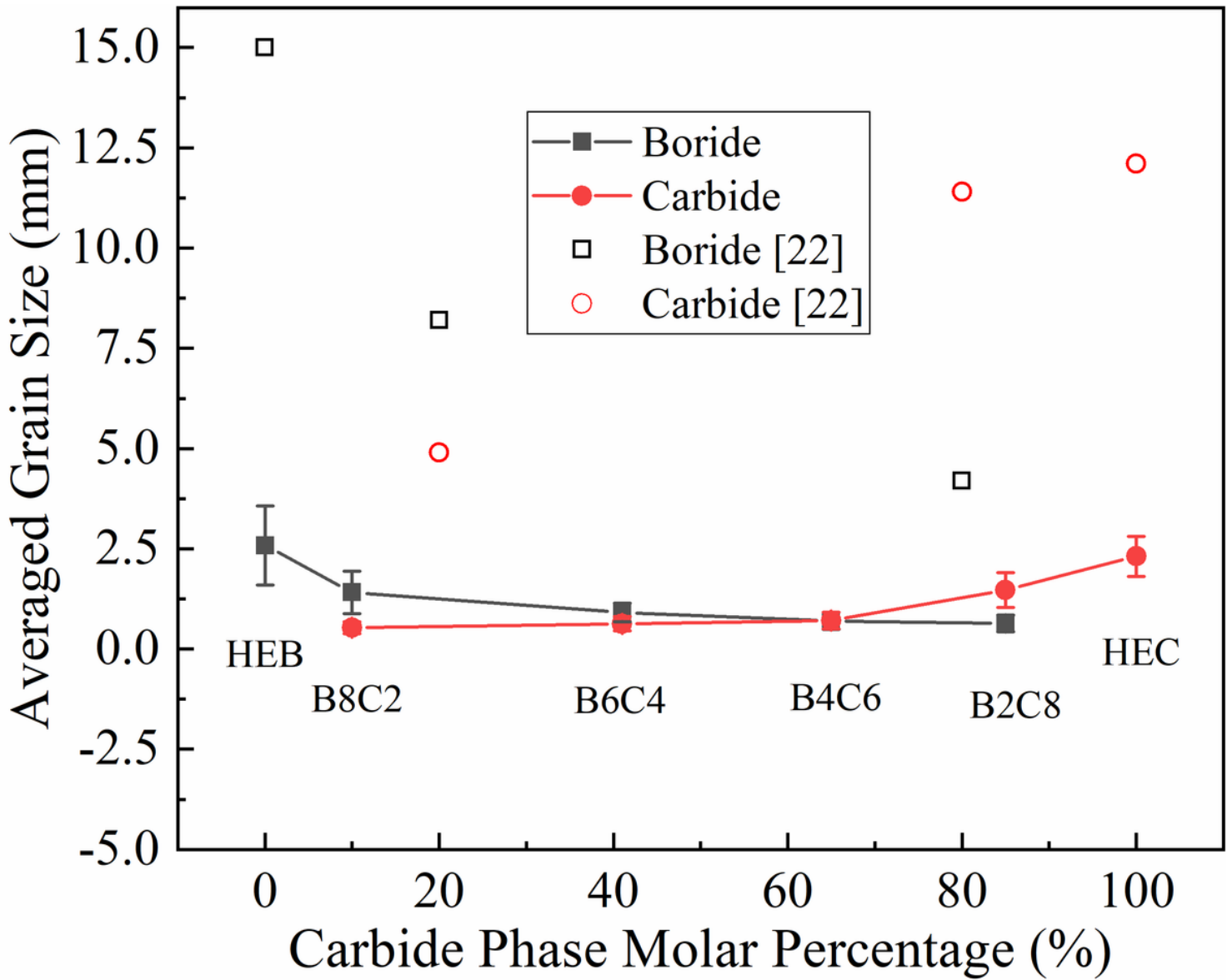


Figure 5

Averaged grain size of the SPS processed high-entropy ceramics.

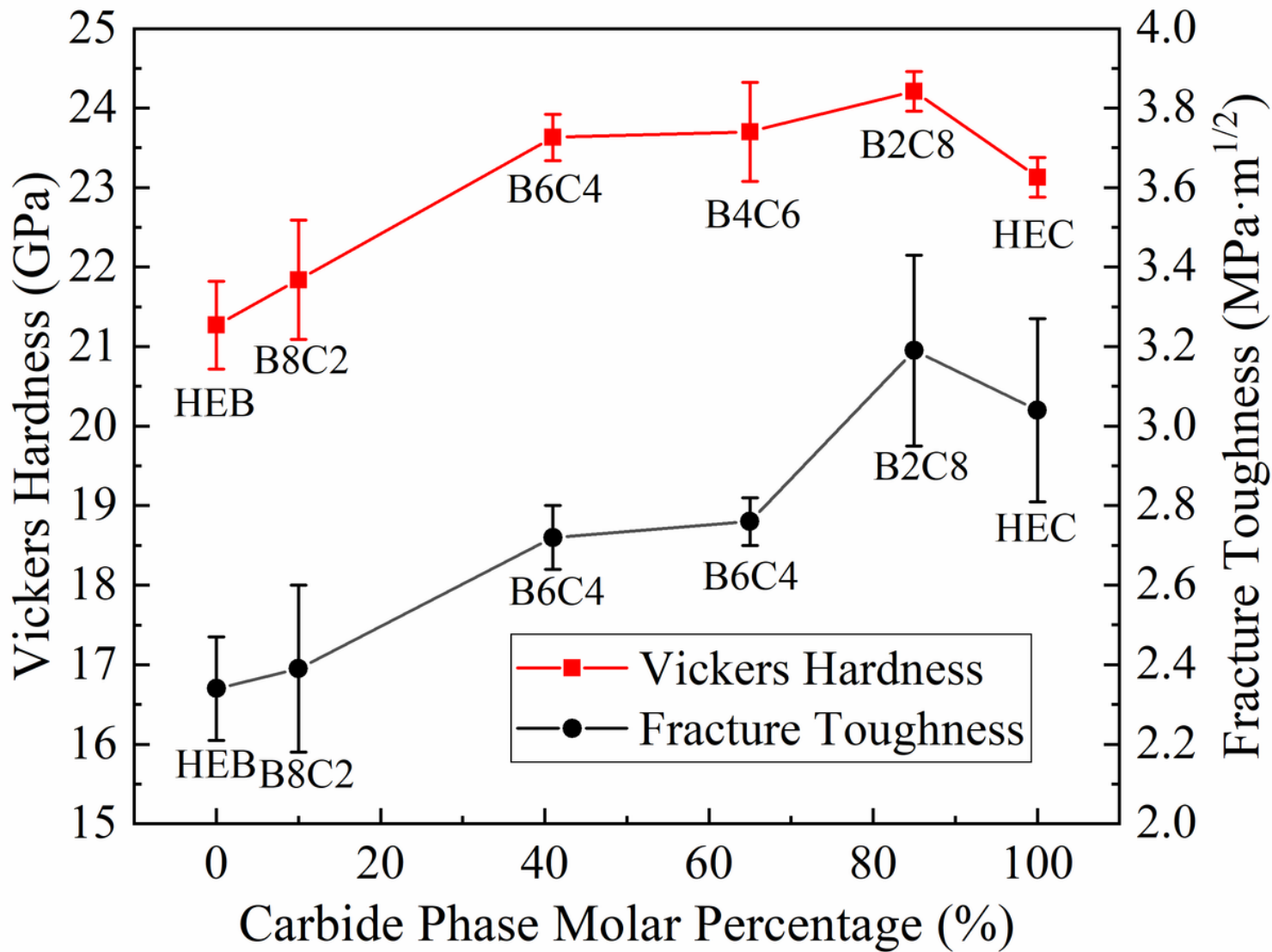


Figure 6

Vickers hardness and fracture toughness of the SPS processed high-entropy ceramics.